Dalton Transactions

ROYAL SOCIETY OF CHEMISTRY

PAPER

View Article Online
View Journal

Cite this: DOI: 10.1039/d5dt01158b

Multi-step spin-crossover in a 2D Hofmann-type clathrate with bisubstituted pyrazine†

Xiangkun Wen, Mengling Wu, Yancong Chen, Yanru Chen, Zhaoping Ni * and Mingliang Tong

Received 16th May 2025,
Accepted 7th July 2025

DOI: 10.1039/d5dt01158b

rsc.li/dalton

Multi-step spin-crossover (SCO) materials, which exhibit multiple distinct spin states, are considered promising candidates for high-order data storage and multiple switches. However, such materials remain rare, necessitating the development of innovative design strategies. Here, we chose an inexpensive asymmetric ligand, 2-chloro-6-methylpyrazine (ClMepz), and synthesized two-dimensional (2D) Hofmann-type clathrates $[Fe(ClMepz)_2\{M(CN)_2\}_2]\cdot ClMepz$ (M = Au (**1**), Ag (**2**)), in which ClMepz serves as a monodentate ligand and a guest molecule. Unlike the two-step SCO behavior in **2**, compound **1** possesses more spin states and exhibits multi-step SCO behavior. The magneto-structural analysis reveals that the more linear $[Au(CN)_2]^-$ unit exerts greater stress on the Hofmann layer, leading to the antiferro-elastic interactions. Additionally, the asymmetric host–guest interactions contribute to the stepwise SCO properties. Thus, the incorporation of asymmetric bisubstituted ligands into 2D Hofmann-type systems represents a viable and cost-effective strategy for the development of multi-step SCO materials.

Introduction

Multistable materials have garnered significant attention due to their potential application in high-order data storage, sensor technologies, and multiple switches.[1,2] As a type of classic bistable material, spin-crossover (SCO) complexes exhibit reversible transitions between low-spin (LS) and high-spin (HS) states in response to external stimuli such as temperature, pressure, light and chemical reagents.[3,4] When elastic frustration arises, the competition between long-range ferro-elastic and antiferro-elastic interactions among SCO units can stabilize intermediate spin states, resulting in multi-step SCO behaviors observed as collective phenomena.[5] However, designing such multi-step SCO systems remains a formidable challenge.

Hysteretic multi-step SCO materials, which display multiple spin states, hold great potential for application in high-order data storage and multiple switches. However, to date, multi-step SCO behaviors remain scarcely observed.[6–12] Hofmann-type clathrates, known since 1897,[13] consist of metal-cyanometallate networks that incorporate guest molecules.[14] Since Kitazawa reported the first Hofmann-type SCO complex in 1996,[15] this class of materials has expanded into a big family within the SCO field.[16–21] According to the elastic model, Hofmann-type networks provide an ideal platform for the manifestation of antiferroelasticity.[22] In 2016, Kepert and co-workers reported the first four-step SCO behavior in a three-dimensional (3D) Hofmann-type metal–organic framework (MOF) $[Fe(bipydz)\{Au(CN)_2\}_2]\cdot 4EtOH$ (bipydz = 3,6-bis(4-pyridyl)-1,2-diazine), which exhibits five spin states with the HS fractions (γ_{HS}) of 0, 1/3, 1/2, 2/3 and 1.[23] In 2017, the strategy of employing a bent pillar ligand was proposed to construct a 3D Hofmann-type MOF $[Fe(4\text{-abpt})\{Ag(CN)_2\}_2]\cdot 2DMF\cdot EtOH$ (4-abpt = 4-amino-3,5-bis(4-pyridyl)-1,2,4-triazole) with the sequence of $\gamma_{HS} = 0 \leftrightarrow 1/4 \leftrightarrow 1/2 \leftrightarrow 3/4 \leftrightarrow 1$, in which the hydrogen-bonding interactions between the host and guest played a crucial role in achieving four-step SCO behavior.[24] Upon replacing the $[Ag(CN)_2]^-$ unit with the $[Au(CN)_2]^-$ linker, an asymmetric seven-/eight-step SCO behavior was observed in $[Fe(4\text{-abpt})\{Au(CN)_2\}_2]\cdot 2DMF\cdot EtOH$.[25] Furthermore, the strategy of combining a bent pillar ligand with host–guest π···π interactions has been employed to explore multi-step SCO properties.[26] However, the synthesis of these pillar ligands is challenging and they are also prohibitively expensive.[23–26]

In addition to 3D MOFs, two-dimensional (2D) coordination polymers also exhibit multi-step SCO behaviors. For example, four-step SCO behaviors with γ_{HS} of 0, 1/6, 4/6, 5/6 and 1 have been observed in 2D Hofmann-type compounds $[Fe_3(saltrz)_6\{M(CN)_4\}_3]\cdot 8H_2O$ (saltrz = (*E*)-2-(((4*H*-1,2,4-triazol-4-yl)imino)methyl)phenol, M = Pt^{II}, Pd^{II}).[27] This observation suggests that cost-effective monodentate ligands can be uti-

Key Laboratory of Bioinorganic and Synthetic Chemistry of Ministry of Education, School of Chemistry, Institute of Green Chemistry and Molecular Engineering, Guangdong Basic Research Center of Excellence for Functional Molecular Engineering, Sun Yat-Sen University, Guangzhou 510275, China.
E-mail: nizhp@mail.sysu.edu.cn

† Electronic supplementary information (ESI) available. CCDC 2428212–2428218. For ESI and crystallographic data in CIF or other electronic format see DOI: https://doi.org/10.1039/d5dt01158b

lized to construct multistable materials.[8,10,28] By analyzing the reported multi-step SCO examples, we found that asymmetric ligands and asymmetric host–guest interactions are crucial for achieving multi-step SCO properties.[10,24–27] Here, we employed a cheap and asymmetrically bisubstituted ligand, 2-chloro-6-methylpyrazine (ClMepz), to construct two new 2D Hofmann-type clathrates: $[Fe(ClMepz)_2\{M(CN)_2\}_2]\cdot ClMepz$ (M = Au (**1**) and Ag (**2**)). Compound **2** only exhibits two-step SCO behavior. In contrast, compound **1** has more spin states and displays multi-step SCO behavior. Hence, this study provides an effective strategy for the development of multi-step SCO materials.

Experimental section

Materials and methods

All the chemical reagents and solvents were commercially available and used without further purification. Powder X-ray diffraction (PXRD) patterns were recorded on a Rigaku Smart lab X-Ray diffractometer with $Cu_{K\alpha}$ radiation (λ = 1.54178 Å) at a scan rate of 5° min^{-1}. Elemental analyses of C, H and N were conducted using an Elementar Vario-EL CHNS elemental analyzer. Fourier transform infrared (FT-IR) spectra were collected in the range of 4000–400 cm^{-1} on a Thermo Nicolet Avtar 330 FT-IR spectrometer. Thermogravimetric (TG) analyses were performed from 25 °C to 800 °C at a heating rate of 10 K min^{-1} using a Netzsch TG209F3 Libra analyzer under a N_2 flow. Differential scanning calorimetry (DSC) measurements were carried out in an aluminum crucible under a nitrogen atmosphere on a Netzsch-200 at a scan rate of 5 K min^{-1}.

Synthetic procedure

$[Fe(ClMepz)_2\{Au(CN)_2\}_2]\cdot ClMepz$ (1). $FeSO_4\cdot 6H_2O$ (0.1 mmol) was dissolved in 4 mL of H_2O and transferred to a test tube. A solution of ClMepz (0.3 mmol) and $K[Au(CN)_2]$ (0.2 mmol) in 4 mL of ethanol was carefully layered on top, separated by a buffer layer (2 mL, $H_2O:EtOH = 1:1$). Yellow block crystals suitable for X-ray diffraction analysis were obtained after one week. Yields: 30%. Anal. calcd for $C_{19}H_{15}Au_2FeN_{10}Cl_3$: C 24.29, H 1.61, N 14.91. Found: C, 24.45; H, 1.66; N, 14.98. IR spectra (ATR, cm^{-1}): 3053 (w), 2169 (m), 1568 (m), 1513(m), 1379(s), 1167(s), 1021 (s), 865 (s), 737 (s), 492(s).

$[Fe(ClMepz)_2\{Ag(CN)_2\}_2]\cdot ClMepz$ (2). Compound **2** was synthesized following a similar procedure to that of compound **1**, with the exception that $K[Ag(CN)_2]$ was used in place of $K[Au(CN)_2]$. Yield: 31%. Anal. calcd for $C_{19}H_{15}Ag_2FeN_{10}Cl_3$: C, 29.97; H, 1.99; N, 18.40. Found: C, 30.00; H, 2.17; N, 18.50. IR spectra (ATR, cm^{-1}): 3051 (w), 2162 (m), 1574 (m), 1515(m), 1388(s), 1182(s), 1016 (s), 873 (s), 731 (s), 480(s).

Magnetic measurements

Magnetic susceptibility measurements were performed on a Quantum Design PPMS3 SQUID magnetometer with a sweep rate of 2 K min^{-1} under an applied field of 5 kOe. Data were corrected for the signal of the sample holder and the diamagnetic contribution was calculated from Pascal's constants.

Single crystal X-ray diffraction

Single-crystal X-ray diffraction data for **1** at 100, 148, 170 and 250 K were collected on a Bruker D8 QUEST diffractometer using $Ga_{K\alpha}$ radiation (λ = 1.34138 Å). Single-crystal X-ray diffraction data for **2** at 170, 240 and 300 K were recorded on a Rigaku Supernova diffractometer with $Cu_{K\alpha}$ radiation (λ = 1.54184 Å). The crystal structures were solved by intrinsic phasing using the SHELXT[29] program and refined *via* least-squares minimization with the SHELXL[30] package in OLEX2.[31] Non-hydrogen atoms were refined with anisotropic displacement parameters, while hydrogen atoms were modeled using a riding model to maintain the idealized geometry. The crystallographic data have been deposited in the Cambridge Crystallographic Data Centre (CCDC) under deposition numbers 2428212–2428218.†

Results and discussion

Slow diffusion of ClMepz and $K[Au(CN)_2]/K[Ag(CN)_2]$ into $FeSO_4\cdot 6H_2O$ in H_2O/EtOH solution resulted in the formation of yellow/orange red block single crystals of **1**/**2**, respectively. Elemental analysis, powder X-ray diffraction and infrared spectral analysis (Fig. S1–4†) were conducted to confirm the purity of the crystalline samples. Thermogravimetric (TG) analysis (Fig. S5 and S6†) indicates that the loss of guest molecules in **1** and **2** begins rapidly after 125 and 140 °C, respectively, followed by the collapse of the framework.

Magnetic properties

Variable-temperature magnetic susceptibility measurements at 2 K min^{-1} revealed multi-step SCO behavior in **1** (Fig. 1a). The $\chi_M T$ value is 3.97 cm^3 K mol^{-1} at 300 K, indicating an HS state for the iron(II) ion (Fig. S7†). It remains nearly constant until 250 K and then gradually decreases upon cooling. An inclined plateau is observed between 175 and 166 K, corresponding to an intermediate $LS_{1/2}HS_{1/2}$ state. The $\chi_M T$ value gradually decreases from 1.97 cm^3 K mol^{-1} at 166 K to 1.03 cm^3 K mol^{-1} at 138 K, with an obscure plateau between them. Then, it abruptly decreases to 0.09 cm^3 K mol^{-1} at 135 K, corresponding to the LS state for the iron(II) ion. Typically, the spin transition temperature $T_{1/2}$ (γ_{HS} = 0.5) can be derived from the temperature-dependent fraction of HS molecules, γ_{HS}. In the case of multi-step SCO behavior, the spin transition temperatures are generally inferred from the 1st derivative of the magnetic data. However, the situation becomes complex when the magnetic plateau is not clearly distinguishable. The 1st derivative of the magnetic data exhibits a sharp peak at 136 K, which is consistent with the abrupt spin transition process. A broad peak emerges at 163 K, which can be attributed to the gradual SCO process observed magnetically. An intermediate $LS_{2/3}HS_{1/3}$ state is deduced, corresponding to the obscure plateau in the low-temperature region. Incorporating the dis-

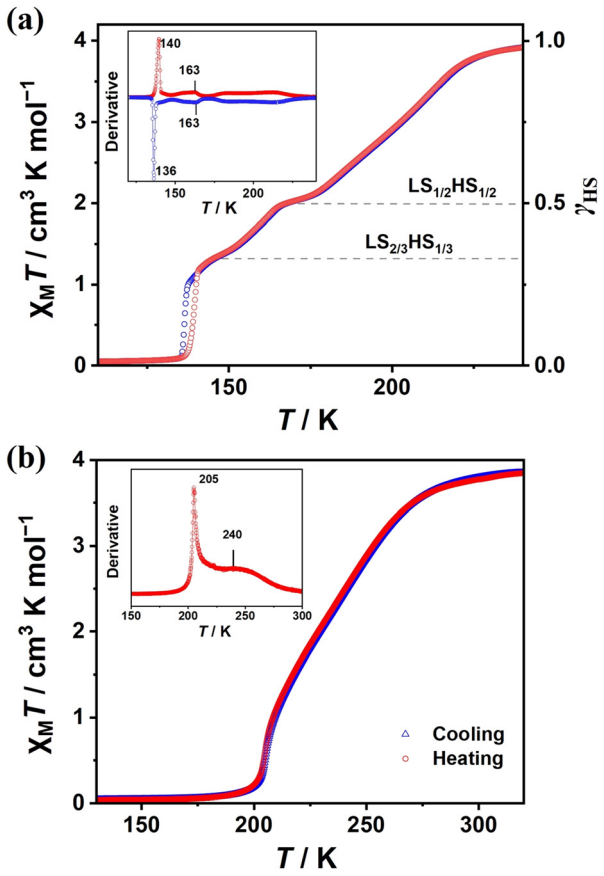

Fig. 1 Variable-temperature magnetic susceptibility data of **1** (a) and **2** (b) at a scan rate of 2 K min^{-1}. Inset: 1st derivative plots of magnetic data. The blue and red points represent the cooling and heating modes, respectively.

tinct LS, $LS_{1/2}HS_{1/2}$ and HS states, compound **1** exhibits four spin states, corresponding to a three-step SCO property. A broad peak is expected to occur at 202 K between $LS_{1/2}HS_{1/2}$ and HS states on the differential magnetic curve. Conversely, it appears that two broad and flattened peaks are present, indicating a hidden four-step SCO behavior. Unfortunately, accurately determining the spin transition temperature is challenging due to the wide and flattened nature of the peaks. The subsequent magnetic curve in the heating mode shows a small hysteresis loop in the abrupt SCO region and almost overlaps in the gradual SCO region. The 1st derivative curve illustrates a sharp peak at 140 K, a broad peak at 163 K and two obscure peaks in the high-temperature region, illustrating a hysteretic multi-step SCO behavior in **1**.

The hysteretic multi-step SCO behaviour is further confirmed by two consecutive cycles of magnetic data at 2 K min^{-1} and the scan rate dependence of magnetic susceptibility measurements (Fig. S7 and S8†). The spin transition curves measured at scan rates of 0.5, 2, 5 and 10 K min^{-1} nearly overlap, indicating the absence of a scan rate effect on the thermal hysteresis in the low-temperature region. Two broad and flattened peaks in the high-temperature region are more distinguishable on the differential magnetic curve at 10 K min^{-1} (Fig. S9†), revealing the nature of the four-step SCO behavior with the sequence of LS ↔ $LS_{2/3}HS_{1/3}$ ↔ $LS_{1/2}HS_{1/2}$ ↔ $LS_{1/3}HS_{2/3}$ ↔ HS. Unfortunately, the magnetic plateau for the $LS_{1/3}HS_{2/3}$ state cannot be clearly discerned from the magnetic susceptibility data.

To corroborate the multi-step SCO behaviour in **1**, DSC measurements were conducted at scan rates of 5 and 20 K min^{-1} (Fig. S10 and S11†). The DSC curves measured at a scan rate of 5 K min^{-1} exhibit a sharp exothermic peak at 136 K and a broad exothermic peak at 162 K in the cooling mode (Fig. S10†), which are consistent with the respective abrupt and gradual SCO processes occurring in the low-temperature region. Meanwhile, endothermic peaks at 139 and 163 K are clearly observed in the heating mode. However, the broad peaks in the high-temperature region cannot be precisely defined. Fortunately, when the scan rate is increased to 20 K min^{-1}, the DSC curves clearly show four exothermic peaks at 135, 157, 183 and 209 K in the cooling mode and four endothermic peaks at 141, 161, 183 and 209 K in the heating mode (Fig. S11†). These values align with the spin transition temperatures of 136, 161, 182 and 212 K in the cooling mode and 140, 161, 182 and 212 K in the heating mode derived from differential magnetic data at 10 K min^{-1} (Fig. S9†). The slight discrepancies between the DSC and magnetic data can be attributed to the different scan rates. Consequently, the concealed four-step SCO behavior is clearly verified by the DSC data at 20 K min^{-1}.

Unlike the multi-step SCO behavior observed in **1**, a two-step SCO behavior is evident in **2** (Fig. 1b). The $\chi_M T$ value gradually decreases from 3.74 cm^3 K mol^{-1} at 320 K to 1.02 cm^3 K mol^{-1} at 210 K, and then rapidly drops to 0.16 cm^3 K mol^{-1} at 198 K, and slightly decreases to 0.02 cm^3 K mol^{-1} at 10 K (Fig. S12†). The 1st derivative curve exhibits a sharp peak at 205 K and a shoulder peak at 240 K, indicating a two-step SCO behavior with the sequence of LS ↔ $LS_{3/4}HS_{1/4}$ ↔ HS. However, no distinct magnetic plateau corresponding to the $LS_{3/4}HS_{1/4}$ state is observed on the magnetic curve. The subsequent heating curve precludes the presence of a thermal hysteresis loop. DSC data at 5 K min^{-1} show one prominent sharp peak at 203 K in the cooling mode and at 207 K in the heating mode (Fig. S13†), corresponding to the abrupt SCO process in the low-temperature region. Meanwhile, a broad peak associated with the gradual spin transition process is observed in the high-temperature region, further confirming the two-step SCO property in **2**.

Structural analysis

To investigate the distinct magnetic behaviors, variable-temperature single-crystal data were collected for **1** at 100, 148, 170 and 250 K and for **2** at 170, 240 and 300 K (Tables S1 and S2, ESI†). Compound **1** crystallizes in the triclinic space group $P\bar{1}$ at 100 K. The asymmetric unit consists of one unique iron(II) ion, two ClMepz ligands, two $[Au(CN)_2]^-$ linkers, and one ClMepz guest molecule (Fig. 2a). The iron(II) ions are connected equatorially by four separate $[Au(CN)_2]^-$ linkers to form

$[Fe\{Au(CN)_2\}_2]_\infty$ 2D layers along the *ab* plane, in which the dimensions of the $[Fe_4\{Au(CN)_2\}_4]$ grid are 10.18 Å and 10.15 Å. Meanwhile, each iron(II) ion is coordinated axially by two monodentate ClMepz ligands, resulting in a 2D Hofmann-type coordination polymer. Consequently, the iron(II) ion is located in a distorted octahedral $[FeN_6]$ environment. The average Fe–N bond length is 1.968 Å at 100 K (Table S3, ESI†), which is typical for iron(II) in the LS state. Due to the steric hindrance from the substituents at the 2- and 6-sites, the nitrogen atom at the 1-site of the pyrazine ligand does not participate in the coordination, thereby preventing the formation of 3D MOFs. This behavior contrasts with that observed in the 3D Hofmann-type MOFs $[Fe(Fpz)\{Au(CN)_2\}_2]$ (Fpz = 2-fluoropyrazine) and $[Fe(Mepz)\{Au(CN)_2\}_2]$ (Mepz = 2-methylpyrazine), where 2Fpz and 2Mepz serve as bridging ligands.[32,33]

As shown in Fig. 2a, the chlorine and methyl substituents are ordered on one ClMepz (L2: Cl2, N7, N8, C10–C14) ligand at 100 K. In contrast, these substituents are disordered on the other ClMepz (L1: Cl1, N5, N6, C5–C9) ligand and the ClMepz (G1: Cl3, N9, N10, C15–C19) guest, occupying 50% of the positions at sites 2 and 6. All three pyrazine units remain ordered. To distinguish the disordered ligand, ordered ligand and disordered guest, they are designated as L1, L2 and G1, respectively. The dihedral angle between two pyrazine units from two coordinated ligands is 8.26° at 100 K. Notably, all ligands above the Hofmann layer are disordered L1, while those below are ordered L2 (Fig. 2b). Consequently, there are no symmetric elements on the Hofmann layer.

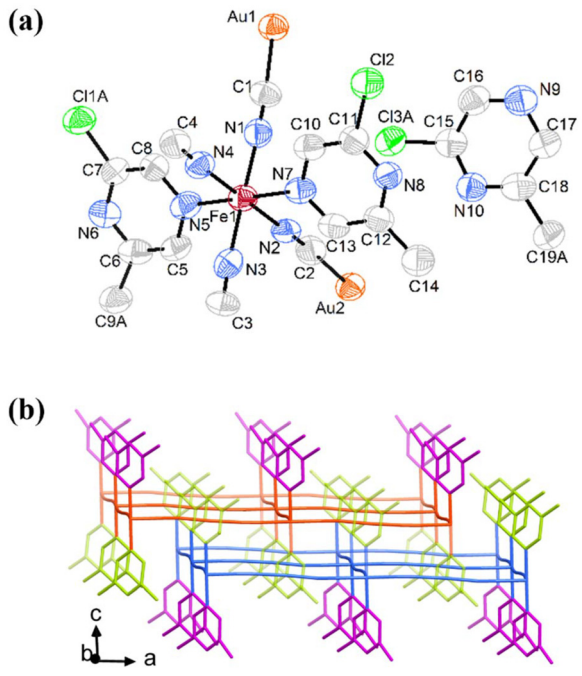

Fig. 2 (a) The asymmetric unit and (b) 2D framework without guest molecules in **1** at 100 K. Thermal ellipsoids are depicted at 50% probability. Hydrogen atoms are omitted for clarity. The L1 and L2 ligands are shown in violet and green, respectively.

Since the $[Fe_4\{Au(CN)_2\}_4]$ grid within the Hofmann layer features a large rhombic window, it is further interpenetrated by one ClMepz ligand from the adjacent lower layer (Fig. 2b and S15†). Consequently, these two Hofmann layers are interwoven in such a manner that each $[Fe_4\{Au(CN)_2\}_4]$ grid in one layer is threaded by one ligand from the opposite layer, in which an inversion center exists between these two Hofmann layers. These paired layers are further stabilized by strong aurophilic interactions, characterized by an interlayer Au···Au distance of 3.072 Å at 100 K.

The incorporation of the ClMepz guest molecule facilitates host–guest interactions both within and between the paired layers in **1** (Fig. 3). Specifically, G1 is situated between the disordered ligand L1 in the upper layer and the ordered ligand L2 in the lower layer (Fig. S16†). An offset face-to-face π···π interaction is observed between G1 and L1, with the centroid distance between the pyrazine rings *Z* being 3.885 Å at 100 K and a dihedral angle θ of 21.14°. The disordered chlorine substituent on G1 participates in Cl–π interaction with the pyrazine ring from L2, where the distance between Cl3A and the centroid of the pyrazine ring is 3.101 Å, and the distance between Cl3A and C11 is 3.296 Å. Given that their difference is less than 0.3 Å, this Cl–π interaction exhibits a "face-on" geome-

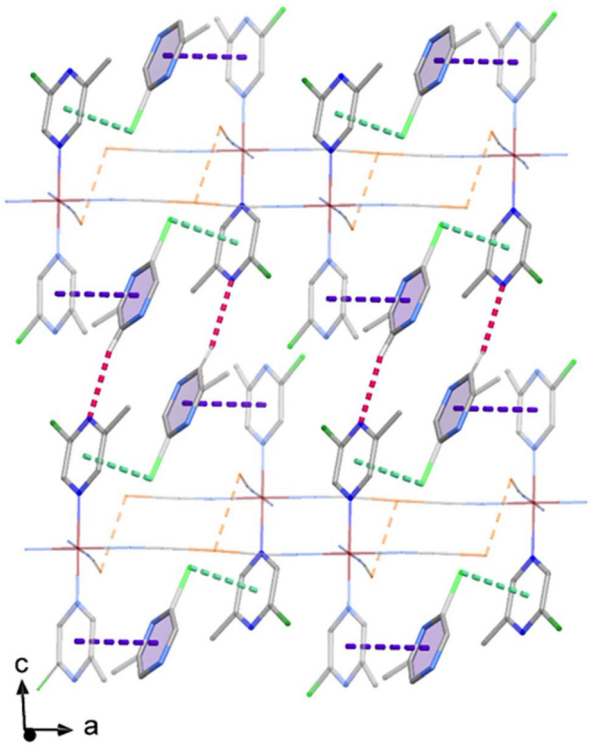

Fig. 3 Host–guest interactions and aurophilic interactions (orange dashed lines) in **1** at 100 K. Offset face-to-face π···π interactions, Cl–π interactions and C–H···N interactions are shown as purple, green and red dashed lines, respectively. Color code: Fe, brown; Au, orange; N, blue; C, gray; H white. Only the H17 atom is shown. L1 and L2 ligands are distinguished by light and dark colors, respectively. The ring of the guest molecule is shown in purple.

try.[34] The chlorine and methyl substituents are disordered at this position with an occupancy ratio of 1 : 1. When the substituent is a methyl group, it engages in CH–π interaction with L2 (Fig. S17†), with the distance between C19B and the centroid of the pyrazine ring being 3.098 Å. Additionally, G1 forms weak hydrogen-bonding interaction with L2 from the adjacent paired layer (C17···N8 = 3.486 Å). The distance between the centroids of pyrazine rings from two nearest guest molecules is 4.414 Å, thereby inhibiting effective guest–guest interactions.

Magneto-structural correlation

To elucidate the stepped SCO behavior, a comprehensive analysis of the structural parameters of **1** was performed. Compound **1** retains the triclinic space group $P\bar{1}$ at 148, 170 and 250 K, with one unique iron(II) ion. The chlorine and methyl substituents are disordered on two independent ligands and one guest molecule. No symmetry breaking is observed at 148 and 170 K, attributed to the narrow magnetic plateaus. The average Fe–N bond lengths are 2.035 and 2.063 Å at 148 and 170 K, respectively, indicative of mixed spin states. It increases to 2.167 Å at 250 K, signifying an HS state. The octahedral distortion parameter Σ provides insight into the stepwise SCO behavior. The Σ values are 12.8, 10.8, 9.9 and 12.0° at 100, 148, 170 and 250 K, respectively. Given that the LS iron(II) ions exhibit smaller Σ values than their HS counterparts, the anomalous Σ value at 148 K suggests the presence of antiferro-elastic interactions, which are essential for the stepwise SCO system according to the elastic model.[12] During the SCO process, the Fe–N bond length and unit cell volume increase monotonically upon heating, leading to a progressive weakening of the offset face-to-face π···π interactions, Cl–π/CH–π interactions and hydrogen-bonding interactions.

Compound **2** crystallizes in the triclinic space group $P\bar{1}$ at 170, 240 and 300 K and exhibits a 2D Hofmann-type structure analogous to that of **1**, with the exception of differing cyanometallate linkers (Fig. S18 and S19†). The average Fe–N bond lengths are 1.965 Å at 170 K and 2.166 Å at 300 K (Table S4, ESI†), corresponding to the LS and HS states, respectively. The absence of a magnetic plateau results in the lack of symmetry breaking in **2** at 240 K, which exhibits an average Fe–N bond length of 2.116 Å corresponding to an intermediate spin state. Upon heating, the Σ value increases from 9.2° at 170 K to 11.2° at 240 K, and then to 12.9° at 300 K. The chlorine and methyl substituents on two distinct ligands and one guest molecule exhibit positional disorder with an occupation ratio of 1 : 1, similar to those observed in **1** at high temperatures. Offset face-to-face π···π interactions, Cl–π/CH–π interactions and hydrogen-bonding interactions in **2** are also comparable to those in **1** (Fig. S20 and S21†), which weaken upon heating.

Despite the structural similarities and analogous host–guest interactions between **1** and **2**, their SCO behaviors exhibit significant differences. The ligand field strength of the cyanide group in the $[Au(CN)_2]^-$ linker is weaker than that in the $[Ag(CN)_2]^-$ linker, resulting in a lower spin transition temperature for **1**. Similar to the distinct stepwise SCO behaviors in $[Fe(4\text{-abpt})\{M(CN)_2\}_2]\cdot 2DMF\cdot EtOH$ (M = Au and Ag),[24,25] the incorporation of the more linear $[Au(CN)_2]^-$ unit imposes greater stress on the iron(II) ion, leading to a more pronounced stepwise SCO behavior. The C–Au–C bond angle (177.6 and 176.4° at 250 K) in **1** is larger than the C–Ag–C bond angle (173.9 and 174.3° at 300 K) in **2**, which accounts for four-step and two-step SCO behaviors, respectively. Furthermore, the incorporation of two distinct substituents leads to asymmetric host–guest interactions, thereby contributing to stepwise SCO behavior.

Conclusions

In summary, we present two 2D Hofmann-type clathrates wherein the asymmetrically bisubstituted pyrazine serves as the monodentate ligand and the guest molecule. The substituents at the 2- and 6-sites introduce steric hindrance to preclude the formation of 3D MOFs. The pyrazine units participate in offset face-to-face π···π interactions and weaker hydrogen-bonding interactions. Meanwhile, the disordered chlorine/methyl substituents engage in the Cl–π/CH–π interactions. These asymmetric host–guest interactions contribute to the stepwise SCO properties. Additionally, the $[Au(CN)_2]^-$ linker is more linear than the $[Ag(CN)_2]^-$ linker, leading to more pronounced stepwise SCO behavior. Consequently, this study provides a straightforward and cost-effective strategy for constructing multi-step SCO materials by utilizing unsymmetrically bisubstituted ligands.

Author contributions

X.-K. Wen performed the experiments and prepared the draft. M.-L. Wu drew the figures. Y.-C. Chen collected and analyzed the magnetic data. Y.-R. Chen collected and refined the crystal data. Z.-P. Ni directed this project and revised the manuscript. M.-L. Tong supervised this project.

Conflicts of interest

The authors declare no conflict of interest.

Data availability

All data are available in the ESI† and from the authors upon request.

Acknowledgements

This work was supported by the NSFC (22488101 and 22271322) and the Fundamental Research Funds for the Central Universities, Sun Yat-Sen University (24xkjc003).

References

1 Y.-J. Zhang, R. Torres-Cavanillas, X.-X. Yan, Y.-X. Zeng, M.-Y. Jiang, M. Clemente-León, E. Coronado and S.-W. Shi, *Chem. Soc. Rev.*, 2024, **53**, 8764–8789.
2 M. Wang, Z.-Y. Li, R. Ishikawa and M. Yamashita, *Coord. Chem. Rev.*, 2021, **435**, 213819.
3 G. Yang, Z.-P. Ni and M.-L. Tong, *Coord. Chem. Rev.*, 2024, **521**, 216146.
4 E. Resines-Urien, E. Fernandez-Bartolome, A. Martinez-Martinez, A. Gamonal, L. Piñeiro-López and J. S. Costa, *Chem. Soc. Rev.*, 2023, **52**, 705–727.
5 M. Paez-Espejo, M. Sy and K. Boukheddaden, *J. Am. Chem. Soc.*, 2016, **138**, 3202–3210.
6 Y. Wu, S. Peng, Z. Zhang, Y. Gao, G. Xu, J. Dai, Z.-Y. Li and M. Yamashita, *Chin. J. Chem.*, 2024, **42**, 879–886.
7 L.-F. Wang, S.-G. Wu, Z.-Y. Ruan, A.-Q. Jian, W. Cui, Z.-P. Ni and M.-L. Tong, *Sci. China: Chem.*, 2023, **66**, 1744–1749.
8 O. I. Kucheriv, S. I. Shylin, V. Y. Sirenko, V. Ksenofontov, W. Tremel, I.-A. Dascălu, S. Shova and I. y. A. Gural'skiy, *Chem. – Eur. J.*, 2022, **28**, e202200924.
9 S.-G. Wu, S. Bala, Z.-Y. Ruan, G.-Z. Huang, Z.-P. Ni and M.-L. Tong, *Chin. Chem. Lett.*, 2022, **33**, 1381–1384.
10 D. J. Mondal, A. Mondal, A. Paul and S. Konar, *Inorg. Chem.*, 2022, **61**, 4572–4580.
11 A. Orellana-Silla, F. J. Valverde-Muñoz, M. C. Muñoz, C. Bartual-Murgui, S. Ferrer and J. A. Real, *Inorg. Chem.*, 2022, **61**, 4484–4493.
12 L. Piñeiro-López, F.-J. Valverde-Muñoz, E. Trzop, M. C. Muñoz, M. Seredyuk, J. Castells-Gil, I. da Silva, C. Martí-Gastaldo, E. Collet and J. A. Real, *Chem. Sci.*, 2021, **12**, 1317–1326.
13 K. A. Hofmann and F. Küspert, *Z. Anorg. Chem.*, 1897, **15**, 204–207.
14 H. M. Powell and J. H. Rayner, *Nature*, 1949, **163**, 566–567.
15 T. Kitazawa, Y. Gomi, M. Takahashi, M. Takeda, M. Enomoto, A. Miyazaki and T. Enoki, *J. Mater. Chem.*, 1996, **6**, 119–121.
16 M. C. Muñoz and J. A. Real, *Coord. Chem. Rev.*, 2011, **255**, 2068–2093.
17 R. Ohtani and S. Hayami, *Chem. – Eur. J.*, 2017, **23**, 2236–2248.
18 Z.-P. Ni, J.-L. Liu, M. N. Hoque, W. Liu, J.-Y. Li, Y.-C. Chen and M.-L. Tong, *Coord. Chem. Rev.*, 2017, **335**, 28–43.
19 K. Otsubo, T. Haraguchi and H. Kitagawa, *Coord. Chem. Rev.*, 2017, **346**, 123–138.
20 B. Kumar, A. Paul, D. J. Mondal, P. Paliwal and S. Konar, *Chem. Rec.*, 2022, **22**, e202200135.
21 M. B. Z. Hegazy, F. Hassan and M. Hu, *Small*, 2024, **20**, 2306709.
22 J. Cruddas and B. J. Powell, *Inorg. Chem. Front.*, 2020, **7**, 4424–4437.
23 J. E. Clements, J. R. Price, S. M. Neville, G. Brown and C. J. Kepert, *Angew. Chem., Int. Ed.*, 2016, **55**, 15105–15109.
24 W. Liu, Y.-Y. Peng, S.-G. Wu, Y.-C. Chen, M. N. Hoque, Z.-P. Ni, X.-M. Chen and M.-L. Tong, *Angew. Chem., Int. Ed.*, 2017, **56**, 14982–14986.
25 Y.-Y. Peng, S.-G. Wu, Y.-C. Chen, W. Liu, G.-Z. Huang, Z.-P. Ni and M.-L. Tong, *Inorg. Chem. Front.*, 2020, **7**, 1685–1690.
26 C.-J. Zhang, K.-T. Lian, G.-Z. Huang, S. Bala, Z.-P. Ni and M.-L. Tong, *Chem. Commun.*, 2019, **55**, 11033–11036.
27 N. F. Sciortino, K. A. Zenere, M. E. Corrigan, G. J. Halder, G. Chastanet, J.-F. Létard, C. J. Kepert and S. M. Neville, *Chem. Sci.*, 2017, **8**, 701–707.
28 K. Kitase, D. Akahoshi and T. Kitazawa, *Dalton Trans.*, 2023, **52**, 2571–2579.
29 G. M. Sheldrick, *Acta Crystallogr., Sect. A: Found. Crystallogr.*, 2008, **64**, 112–122.
30 G. M. Sheldrick, *Acta Crystallogr., Sect. C: Struct. Chem.*, 2015, **71**, 3–8.
31 O. V. Dolomanov, L. J. Bourhis, R. J. Gildea, J. A. K. Howard and H. Puschmann, *J. Appl. Crystallogr.*, 2009, **42**, 339–341.
32 F. J. Valverde-Muñoz, M. Seredyuk, M.-C. Muñoz, K. Znovjyak, I. O. Fritsky and J. A. Real, *Inorg. Chem.*, 2016, **55**, 10654–10665.
33 S. I. Shylin, O. I. Kucheriv, S. Shova, V. Ksenofontov, W. Tremel and I. y. A. Gural'skiy, *Inorg. Chem.*, 2020, **59**, 6541–6549.
34 Y. N. Imai, Y. Inoue, I. Nakanishi and K. Kitaura, *Protein Sci.*, 2008, **17**, 1129–1137.